Article

Molecular Dynamics Simulations and MM/PBSA Analysis of Annocatacin B in ND1 Subunit of Human Mitochondrial Respiratory Complex I

Camilo Febres-Molina [1]; Jorge A. Aguilar-Pineda [1,2]; Pamela L. Gamero-Begazo [1]; Haruna L. Barazorda-Ccahuana [1]; Diego E. Valencia [1]; Karin J. Vera-López[2,4]; Gonzalo Davila-Del-Carpio[3,4], and Badhin Gómez *,1,4

1   Centro de Investigación en Ingeniería Molecular - CIIM, Universidad Católica de Santa María, Urb. San José s/n - Umacollo, Arequipa, Perú
2   Laboratory of Genomics and Neurovascular Diseases, Vicerrectorado de Investigación, Universidad Católica de Santa María, Arequipa, Peru.
3   Vicerrectorado de Investigación, Universidad Católica de Santa María, Arequipa, Perú.
4   Facultad de Ciencias Farmacéuticas, Bioquímicas y Biotecnológicas, Universidad Católica de Santa María, Urb. San José s/n - Umacollo, Arequipa, Perú
*   Correspondence: bgomez@ucsm.edu.pe; Tel.: +51-982895967

1   **Abstract:** ND1 subunit possesses the majority of the inhibitor binding domain of the human
2   MRC-I. This is an attractive target for the search for new inhibitors that seek mitochondrial
3   dysfunction. It is known, from *in vitro* experiments, some metabolites from *Annona muricata* called
4   acetogenins have important biological activities such as anticancer, antiparasitic, and insecticide.
5   Previous studies propose an inhibitory activity of bovine MRC-I by bis-THF acetogenins such
6   as annocatacin B, however, there are few studies on its inhibitory effect on human MRC-I. In
7   this work, we evaluate the molecular and energetic affinity of the annocatacin B molecule with
8   the human ND1 subunit in order to elucidate its potential capacity to be a good inhibitor of this
9   subunit. For this purpose, QM optimizations, MD simulations and MM/PBSA analysis were
10   performed. As a control to compare our outcomes, the molecule rotenone, which is a known
11   MRC-I inhibitor, was chosen. Our results show that annocatacin B has a greater affinity for the
12   ND1 structure, its size and folding were probably the main characteristics that contributed to
13   stabilize the molecular complex. Furthermore, the MM/PBSA calculations showed a 35% stronger
14   BFE compared to the rotenone complex. Detailed analysis of the BFE shows that the aliphatic
15   chains of annocatacin B play a key role in molecular coupling by distributing favorable interactions
16   throughout the major part of the ND1 structure. These results are consistent with experimental
17   studies that mention that acetogenins may be good inhibitors of MRC-I.

18   **Keywords:** Annocatacin B, ND1 subunit, mitochondrial respiratory complex I, MRC-I, molecular
19   dynamics simulations, MD, Hirshfeld charges, MM/PBSA

1. Introduction

21   It has been almost 100 years since Warburg presented the first connection between
22   the mitochondria and tumors appearance [1]. The mitochondria fulfill an energetic role
23   in cells, specifically in cancer cells; this role is essential for developing tumors through
24   glycolysis [2,3]. On that basis, several mechanisms associated with tumor generation,
25   such as loss of enzymatic function, mitochondrial genome mutation, reprogramming of
26   mitochondrial metabolism, have been studied [4,5]. Some hypotheses and studies show
27   that, to a greater or lesser extent, neoplastic cells have many phenotypes related to their
28   energy production, from high aerobic glycolysis, through a partially active oxidative
29   phosphorylation, to a highly productive one [6,7]. Although this issue is controversial [8].

30   For instance, the mitochondrial respiratory complex I (MRC-I) is directly involved
31 in the appearance of colorectal cancer [9], prostate cancer [10], endometrial cancer [11],
32 breast cancer [12], and melanoma [13]. Thus, this complex protein has become a thera-
33 peutic target to develop anticancer drugs. Besides, the MRC-I catalyze the formation of
34 reactive oxygen species (ROS).

35   MRC-I, also named ubiquinone oxidoreductase , has a molecular mass of approxi-
36 mately 1 MDa; its structural conformation is composed by fourteen central subunits. ND1
37 subunit is one of those and has most of the inhibitor binding domain in the ubiquinone
38 oxidoreductase. The main inhibitor of the MRC-I is the rotenone molecule. [14]. It is
39 an isoflavone compound and has been found in many *Fabaceae* plants. Furthermore,
40 it was used as a pesticide and piscicide [15] due to its high toxicity [16,17]. Its effect
41 on cancer cell lines has been evaluated *in vitro*, showing inhibition of proliferation and
42 induction of apoptosis [18,19]. Nevertheless, its toxicity in cells complicates its use as an
43 anticancer drug, mainly because it is highly neurotoxic due to its lipophilic nature and
44 also the fact that it does not need an extra metabolism to be active or transporter to enter
45 neurons [14,20,21] Consequently, the challenge is to find new inhibitors that could be
46 less toxic than rotenone.

47   Murai *et al.* analyzed rotenone and a synthetic acetogenin as an inhibitor of the
48 bovine heart MRC-I [22]. They revealed that acetogenins are involved in the binding
49 domain of several inhibitors as rotenone does.In fact, acetogenins with two adjacent
50 tetrahydrofurans (THF) rings were reported to show higher antitumor activity and
51 toxicity than those that had only one THF [23], and have been found in the family of
52 *Annonaceae*, i.e., soursop (*Annonamuricata*) [24].

53   In traditional medicine, soursop also has important uses, including anticonvulsant,
54 antiarthritic, antiparasitic, hepatoprotective, etc. Many of these beneficial attributes have
55 been ascribed to acetogenins [24,25]. One of the most studied properties in soursop is its
56 potential anticarcinogenic effect due, in a way, to its powerful cytotoxic features [25,26].
57 It has been possible to isolate more than 100 acetogenins from different parts of the
58 *Annonaceae* plants [24,25,27]. The effect of acetogenins as inhibitors of the MRC-I has
59 been suggested and demonstrated for more than 20 years [28].

60   Acetogenins have showed important behaviors when evaluating their potential
61 cytotoxic activity against cancer cells; some of these molecules already have proven
62 anti-cancer properties such as bullatacin, motrilin, assimin, trilobacin, annonacin, gi-
63 anttronenin, and squamocin. However, we still do not have enough information about
64 most of the acetogenins [29]. The main characteristic of acetogenins' molecular structure
65 is their linear 32 to 34 carbon chains containing oxygen-containing functional groups.
66 Annocatacin B is an acetogenin with two adjacent THF rings and has been identified in
67 the leaves of soursop; it has also been reported that it possesses toxicity against human
68 hepatoma cells [24,30]. Currently, there is not much information about annocatacin B;
69 so it has a great potential for new research. In that sense, the objective of this work
70 was to determine the plausible inhibitory role of annocatacin B with the ND1 subunit
71 compared with rotenone as a control. Considering all this as a challenge in the search
72 for new inhibitors of MRC-I. To accomplish this, we applied computational techniques
73 as quantum mechanics (QM) calculations, molecular dynamics (MD) simulations, and
74 MM/PBSA calculations.
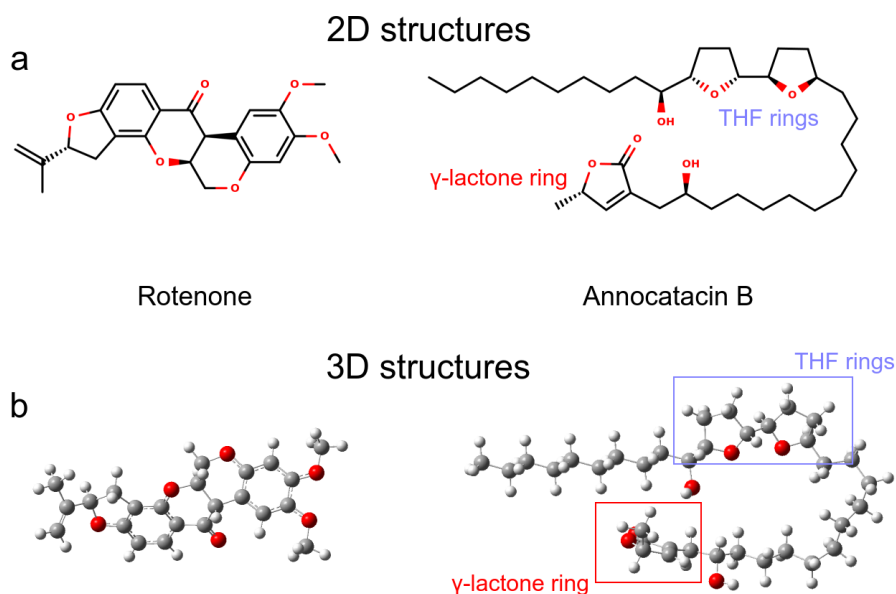
2. Computational Details

Figure 1. Ligand molecules used in this work. (a) 2D representations. (b) 3D representations obtained after QM optimization.

2.1. Structural Preparation

We analyzed two molecules as ligands to the ND1 complex, rotenone (PubChem ID 6758) and annocatacin B (PubChem ID 10483312) (Figure 1a). The structures of both molecules were built using GaussView v.6 software package [31], and optimized by DFT calculations using Gaussian 16 software package [32] (Figure 1b). The optimization process were performed using the CAM-B3LYP exchange-correlation functional [33], and the TZVP basis set [34]. The vibrational frequencies were calculated to ensure that the geometries were those of the minimum energy. In order to investigate the electrostatic effect of the ligands on ND1 complex, atomic charges were calculated using the Hirshfeld population analysis [35–37], and molecular Electrostatic Potential (ESP) surfaces were used to visualize the polar and non polar regions of these ligands. To obtain the MD parameters and topologies of the ligands, we used the TPPMKOP server [38], which uses the parameters of the OPLS-AA force field to generates them [39,40]. These topologies were reparametrized using the optimized structures and atomic charges obtained in previous quantum calculations.

On the other hand, the phospholipid bilayer membrane was built with 512 dipalmitoyl-phosphatidylcholine (DPPC) molecules. A 128-DPPC bilayer with 64 lipid molecules in each layer was replicated four times (two times in both the x and y directions), to obtain the membrane model. The InflateGRO methodology was used for the embedding of ND1 protein in the lipid membrane [41].

The three-dimensional crystallographic structure of the human MRC-I was considered for this study and obtained from the Protein Data Bank (PDB) by the PDB ID: 5XTD [42]. Crystallographic water molecules were removed in Chimera UCSF 1.11.2 [43]. From this MRC-I, the structure of the ND1 subunit was extracted, since it largely possesses the quinone-binding domain between residues Y127 to K262 (according to the ND1 subunit nomenclature).

2.2. MD Simulations

Molecular dynamics (MD) simulations were carried out in Gromacs 2019 [44] with the OPLS-AA force field. Firstly, we performed an energy minimization of the whole

¹⁰⁵ protein in the vacuum with the steepest descent algorithm with a maximum of 50000
¹⁰⁶ steps. Then, the DPPC parameters for the lipid bilayer were obtained from the work
¹⁰⁷ of Peter Tieleman *et al.* [45]. The new system (protein + DPPC membrane) was located
¹⁰⁸ in the center of a cubic box with a 1.0 *nm* distance between the system-surface and the
¹⁰⁹ box edge on z axis. SPC water-model molecules and ions were added to neutralize the
¹¹⁰ systems. Next, we proceeded with another energy minimization with a maximum of
¹¹¹ 50000 steps. The equilibrium MD simulation was realized with position restraint in two
¹¹² ensembles. The first was the canonical ensemble (NVT) at 323.15 K with a trajectory of
¹¹³ 50 *ps* using a V-rescale thermostat. The second was the isobaric-isothermal ensemble
¹¹⁴ (NPT) at 309.65 K, with semi-isotropic pressure coupling, the compressibility of $4.5x10^{-5}$,
¹¹⁵ and a reference pressure of 1.0 bar for along the 50 *ps* of the trajectory using the Nosé-
¹¹⁶ Hoover thermostat and the Parrinello-Rahman barostat. The production of MD without
¹¹⁷ position restrain was calculated in the isobaric-isothermal ensemble at 309.65 K and
¹¹⁸ semi-isotropic pressure coupling (same equilibrium condition of NPT ensemble) for
¹¹⁹ 500 *ns* of trajectory. Periodic boundary conditions (PBC) in all directions, Particle Mesh
¹²⁰ Ewald (PME) algorithm for long-range electrostatics with cubic interpolation with a
¹²¹ cut-off of 0.9 *nm*, and Linear Constraint Solver (LINCS) with all bonds constrained were
¹²² applied for all MD simulations.

2.3. Molecular docking calculations

¹²⁴   First, the coupling was made between the ND1 subunit and rotenone, and then,
¹²⁵ between ND1 and annocatacin B. To accomplish this, we used PATCHDOCK server [46,
¹²⁶ 47] a molecular docking algorithm based on shape complementarity principles, and
¹²⁷ we selected the top score solution for each of the two systems, because these top score
¹²⁸ structures were in agreement with the experimental data. 4.0Å clustering RMSD and
¹²⁹ default mode parameters were used. Later, we took these top score solution complexes
¹³⁰ and introduced them into the lipid bilayer/water systems. Subsequently, we carried out
¹³¹ the MD simulations of the systems: ND1 - rotenone and ND1 - annocatacin B, following
¹³² the aforementioned steps.

2.4. MM/PBSA calculations

¹³⁴   To evaluate the binding affinities of ND1-ligand interactions, we performed the
¹³⁵ Molecular Mechanics Poisson-Boltzmann Surface Area (MM/PBSA) calculations [48].
¹³⁶ Based on the g_mmpbsa program [49]. Calculations of free energies and energy contri-
¹³⁷ butions by residue were carried out in order to localize the main residue interactions
¹³⁸ and to assess the effect of each residue on the ND1 - ligand complexes. The last 200 *ns*
¹³⁹ of the MD trajectories were analyzed at a 1 *ns* time interval to estimate the binding free
¹⁴⁰ energy (ΔG_{bind}) which was calculated by the following equation:

$$\Delta G_{bind} = G_{complex} - (G_{ND1} + G_{lig}) = \Delta E_{MM} + \Delta G_{sol} - T\Delta S \qquad (1)$$

¹⁴¹   where $G_{complex}$ is the total free energy of the ND1-ligand complexes; G_{ND1} and
¹⁴² G_{lig}, are the free energies of isolated ND1 structure and rotenone or annocatacin B in
¹⁴³ solvent. ΔE_{MM}, represents the molecular mechanics energy contibutions; ΔG_{sol} is the
¹⁴⁴ free energy solvation requiered to tranfer a solute from vacuum into the solvent. The
¹⁴⁵ TΔS term refers the entropic contribution and was not included in this calculation due
¹⁴⁶ to the computational costs [49–51]. Therefore, individual E_{MM}, and G_{sol} terms were
¹⁴⁷ calculated as follow:

$$E_{MM} = E_{bonded} + E_{vdW} + E_{elec} \qquad (2)$$

$$G_{sol} = G_p + G_{np} = G_p + \gamma A \qquad (3)$$

¹⁴⁸   In equation 2, the bonded interactions are represented by the E_{bonded} term, and in
¹⁴⁹ the single-trajectory approach, ΔE_{bonded} is taken as zero [48]. The nonbonded interactions

150 are represented by the E_{vdW} and E_{elec} terms. In equation 3, the solvation free energy of
151 (G_{sol}), is the sum of the polar (G_p) and non polar (G_{np}) contributions. The G_p term, is
152 calculated by solving de Poisson-Boltzmann equation, while the G_{np} term, we used de
153 SASA nonpolar model. For our calculations, at 309.65 K, we used the default polar and
154 nonpolar parameters [49]. Finaly, the binding energy by residue was obtained using:

$$\Delta G_{bind}^{res} = \Delta E_{MM}^{res} + G_p^{res} + G_{np}^{res} \qquad (4)$$

155 *2.5. Structure and data analysis*

156   Statistical results, RMSD, RMSF, RG, SASA, hydrogen bonds, free energies, matches,
157 structures, trajectories, B-factor maps, were obtained using Gromacs modules. Analysis
158 of structure properties was performed using the MD trajectories of the last 200 *ns* of each
159 simulations, then visualized using Visual Molecular Dynamics (VMD) software [52] and
160 UCSF Chimera v.1.14 [43]. The graphs were plotted using XMGrace software [53]. 2D
161 representations of electrostatic and hydrophobic interactios were built using LigPlot pro-
162 gram [54]. The ESP surfaces within the molecular mechanics framework were calculated
163 in APBS (Adaptive Poisson Boltzmann Surface) software v.1.4.1, [55] and the pqr entry
164 was created in the PDB2PQR server [56]. Free Energy Landscape (FEL) maps were used
165 to visualize the energy associated with the protein conformation of the different models
166 during the MD simulations. These maps are usually represented by two variables related
167 to atomic position and one energetic variable, typically the Gibbs free energy. In this
168 work, we considered two substructures of ND1 protein for the FEL map analysis, Site A
169 (Y127 to F198) and Site B (D199 to K262), these two regions were adopted from the work
170 of Kakutani *et al.* [57]. The FEL maps were plotted using *gmx sham* module while the
171 RMSD and radius of gyration were considered as the atomic position variables respect to
172 its average structure and figures were constructed using Wolfram Mathematica 12.1 [58].

173 **3. Results and discussion**

174   The human MRC-I belong to a highly organized supercomplex, named respirasome.
175 The complexes I, III, and IV arise more stability at that supercomplex and have the special
176 task of channeling electrons effectively through the electron transport chain [59]. Never-
177 theless, Guo *et al.* proposed an even larger system called megacomplex that includes
178 complex II at the previous respirasome [42]. They suggested that a quinone/quinol
179 (oxidized/reduced forms of the same molecule) pool maximize the oxide-reduction reac-
180 tions. Recent studies suggest there are around 100 Å between complex I and complex
181 III when actively translocating electrons, proposing with this that there is no need for a
182 mediating protein to help the electron channeling through these complexes [42,60].
183   MRC-I is the first in the mega-complex that encounters the quinone site to start the
184 oxide-reduction process. This complex is composed of several subunits, and mainly the
185 ND1 subunit is the one that possesses the majority of the quinone binding domain and,
186 to a lesser extent, the ND3, PSST, and 49 kDa subunits. Fiedorczuk *et al.* studied the
187 open and close positions of the above-mentioned complex I to be active and inactive,
188 respectively [61]. The ND1 subunit has a predominantly structural conformation of
189 alpha-helices that provides the hydrophobic environment expected of a membrane
190 protein and owns the quinone binding domain which is in its core (Table 1).

Table 1: Secondary structure summary

System	Strand	Alpha helix	3-10 helix	Other	Total residues
ND1	0 (0.0%)	154 (48.4%)	9 (2.8%)	155 (48.7%)	318
ND1 - Annocatacin B	0 (0.0%)	129 (39%)	28 (8.8%)	166 (52.2%)	318
ND1 - Rotenone	0 (0.0%)	148 (46.5%)	11 (3.5%)	159 (50.0%)	318

3.1. Structural analysis

3.1.1. Rotenone and Annocatacin B

Before performing the MD simulations, we carried out QM calculations to obtain the optimized structures and analyze the electrostatic properties of the ligand molecules. Figure 1a shows the 2D representation of the ligands, where we can visualize that annocatacin B is larger than rotenone. The optimized structure of annocatacin B shows a closed isoform between the THF rings and the γ-lactone ring (Figure 1b). This result is in agreement with what observed by Nakanishi *et al.*, who reported that the hydrophobic alkyl tail of the acetogenins, in general, looks to serve as a spacer to accommodate the polar hydroxylated bis-THF motif to the polar-membrane part, and its apolar counterpart, the γ-lactone ring, into the core of the lipid bilayer [62].

Both ligand molecules have an electrophilic character and one of the major goals of this study was aimed to assess the electrostatic effect of the ligands on the ND1 structure. Figure 2, shows the quantum and classical ESP surfaces of annocatacin B and rotenone molecules obtained from Hirshfeld population analysis. We can observe that the annocatacin B structure has a high electron density region over the γ-lactone ring and it decreases at the THF rings (Figure 2a). On the other hand, as can be seen from the ESP surface of the rotenone molecule, the high electron density sites are close to the carbonyl group, and the oxygen atoms, as expected (Figure 2b). With these charges, and using the OPLS/AA parameters, we built the annocatacin B and rotenone force fields for the MD simulations. The calculation of the Hirshfeld's atomic charges and their use in molecular mechanics (MM) force fields has been employed in many liquid solvents studies [63–67]. The main advantages of these atomic charges are not to overestimate the electrostatic properties and accelerate the MD calculations.
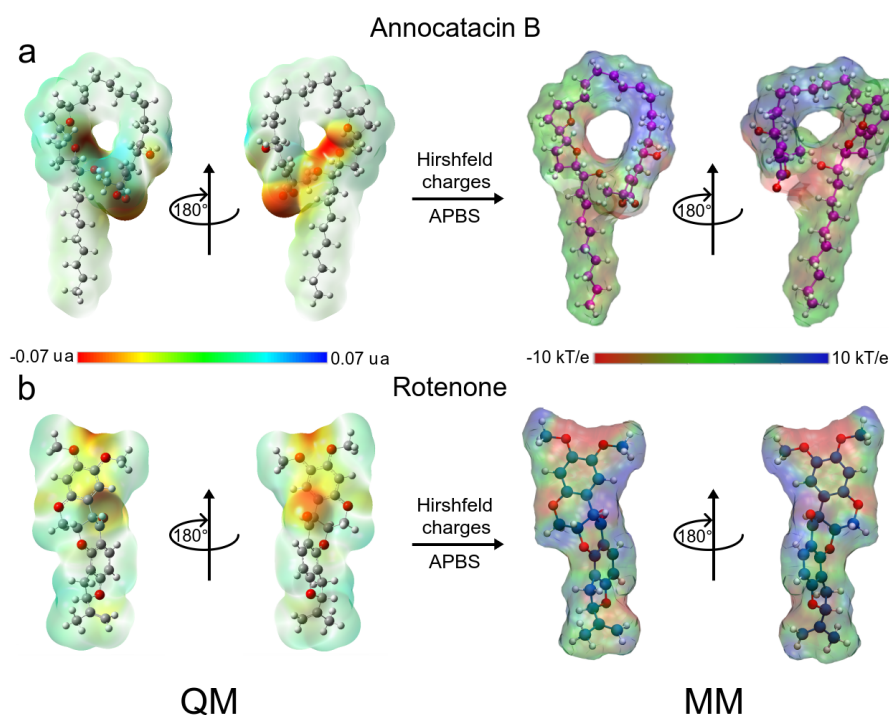

Figure 2. Chemical structure of Annocatacin B and Rotenone molecules. Calculated molecular ESP surfaces of (a) annocatacin B, and (b) rotenone. In the left panel, ESP surfaces obtained at the DFT level using the CAM-B3LYP/TZVP method. In the right panel, ESP surfaces obtained with APBS methodology and the Hirshfeld's atomic charges. On all surfaces, the different colors indicate their molecular electrostatic properties; red for the most nucleophilic zones; dark blue for the most electrophilic zones, and green for the neutral zones.

215   Additionally, the drug-like properties of annocatacin B and rotenone have the
216 following values: six hydrogen bond acceptors in both of them; hydrogen bond donors of
217 2 and 0; molecular weight of 578.875 g/mol and 394.423 g/mol; the number of rotational
218 bonds of 23 and 3; partition coefficient LogP of 8.1069 and 3.7033, and a surface area of
219 250.531 $Å^2$ and 168.525 $Å^2$, respectively. These results confirmed that both molecules are
220 very hydrophobic, being annocatacin B more lipophilic than rotenone, due mostly to its
221 alkyl chain.
222   The pharmacokinetic properties of absorption, distribution, metabolism, excretion,
223 and toxicity (ADMET) are in Table 2. The absorption is similar in both compounds;
224 however, rotenone is not a P-glycoprotein substrate giving a slim advantage to the other
225 molecule. The distribution property is slightly higher for rotenone, which implies that its
226 distribution in the human body (tissues) is a bit greater than annocatacin B. Regarding
227 metabolism, both could be substrates of the CYP3A4 protein, but only rotenone could
228 act as an inhibitor. The excretion and toxicity of these molecules are similar in both
229 cases. In general terms, this description shows that both rotenone and annocatacin B
230 have very similar properties. The pharmacokinetic and toxicological properties of these
231 compounds were analyzed through the pkCSM server [68].

Table 2: ADMET prediction of annocatacin B and rotenone by pkCSM server.

ADMET			
Property	**Model Name**	**Predicted Value**	
		Annocatacin B	**Rotenone**
Absorption	Water solubility[a]	-5.847	-5.054
Absorption	Caco2 permeability[b]	0.402	1.31
Absorption	Intestinal absorption[c]	86.982	99.631
Absorption	Skin Permeability[d]	-2.697	-2.754
Absorption	P-glycoprotein substrate	Yes	No
Absorption	P-glycoprotein I inhibitor	Yes	Yes
Absorption	P-glycoprotein II inhibitor	Yes	Yes
Distribution	VDss (human)[e]	-0.291	-0.044
Distribution	Fraction unbound (human)[f]	0.045	0
Distribution	BBB permeability[g]	-0.949	-0.869
Distribution	CNS permeability[h]	-2.902	-2.818
Metabolism	CYP2D6 substrate	No	No
Metabolism	CYP3A4 substrate	Yes	Yes
Metabolism	CYP1A2 inhibitior	No	Yes
Metabolism	CYP2C19 inhibitior	No	Yes
Metabolism	CYP2C9 inhibitior	No	Yes
Metabolism	CYP2D6 inhibitor	No	No
Metabolism	CYP3A4 inhibitor	No	Yes
Excretion	Total Clearance[i]	1.601	0.195
Excretion	Renal OCT2 substrate	No	No
Toxicity	AMES toxicity	No	No
Toxicity	Max. tolerated dose (human)[j]	-0.644	0.162
Toxicity	hERG I inhibitor	No	No
Toxicity	hERG II inhibitor	No	No
Toxicity	Oral Rat Acute Toxicity (LD50)[k]	3.028	2.869
Toxicity	Oral Rat Chronic Toxicity (LOAEL)[l]	0.786	1.422
Toxicity	Hepatotoxicity	No	No
Toxicity	Skin Sensitisation	No	No
Toxicity	T.Pyriformis toxicity[m]	0.312	0.348
Toxicity	Minnow toxicity[n]	-1.888	-0.333

[a] In log mol/L; [b] In log Papp in 10^{-6} cm/s; [c] In % Absorbed; [d] In log Kp; [e] In log L/kg; [f] In Fu; [g] In log BB; [h] In log PS; [i] In log ml/min/kg; [j] In log mg/kg/day; [k] In mol/kg; [l] In log mg/kg_bw/day; [m] In log ug/L; [n] In log mM.

3.1.2. ND1 - ligand complexes and Stability Descriptors

As we said earlier, ND1 subunit is located in the transmembrane region of human MRC-I [42]. In order to understand the ligand effect on its structure, we carried out MD simulations of a full-length ND1 subunit and its ND1-ligand complexes. To obtain the molecular systems, we isolated the ND1 protein of the MRC-I and was embedded inside a phospholipid bilayer (Figure 3a). As said before, according to Kakutani *et al.*, the ND1 subunit has two regions in the active site, Y127 to F198 (site A) and D199 to K262 (site B), which are involved in the quinone binding domain (Figure 3b) [57]. The authors suggest that natural acetogenins prefer to accommodate more likely in site A and synthetic molecules in site B.
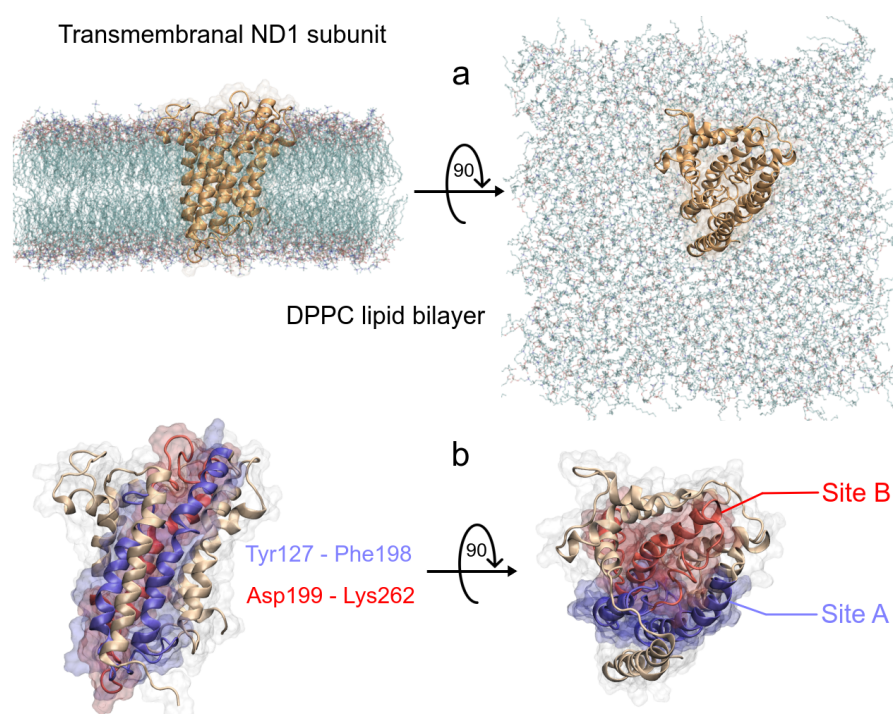

Figure 3. Schematic representation of the ND1 - DPPC membrane complex, (a) initial distribution of the simulated model used in the MD simulation, the lengths of the simulation box are lx = 11.66 *nm*, ly = 11.71 *nm* and lz = 13.02 *nm*. (b) Front and top views of the active site of ND1 protein, in purple color, the active site A, and in red color, the active site B.

Before studying the structural and energy changes of ND1 protein, it was necessary to assess the stability of the molecular complexes during MD simulations. For this purpose, we calculated and plotted the root mean square deviation (RMSD) of the ND1 subunit for all complexes, with respect to its equilibrated structure. Due to the movement restrictions of the lipid bilayer on the ND1 atoms, we observed that there is no significant difference between the protein containing the ligands and the one that does not have them. Specifically, the average RMSD of the last 300 *ns* of the ND1 without ligands was 0.40 ± 0.04 *nm*, and the average RMSD of the last 200 *ns* of ND1 with ligands was 0.48 ± 0.02 *nm* and 0.44 ± 0.02 *nm* for the systems ND1-rotenone and ND1-annocatacin B, respectively. At a glance, we can notice that the last 200 *ns* in the three systems are specially stabilized, that is, within range of the 0.2 *nm* (2 Å) of deviation permitted. However, when we analyzed the final MD structures, we observed a structural impact of the ligands in the active site (Figure 4a). In both ND1-ligand complexes, the ND1 subunit shows an open conformation to allow ligand stability (Figure 4b, 4c). In the case of the rotenone complex, the addition of this ligand caused a structural instability

257 observed in the RMSD of the active site, 0.41 ± 0.11 *nm* against 0.30 ± 0.06 *nm* of the
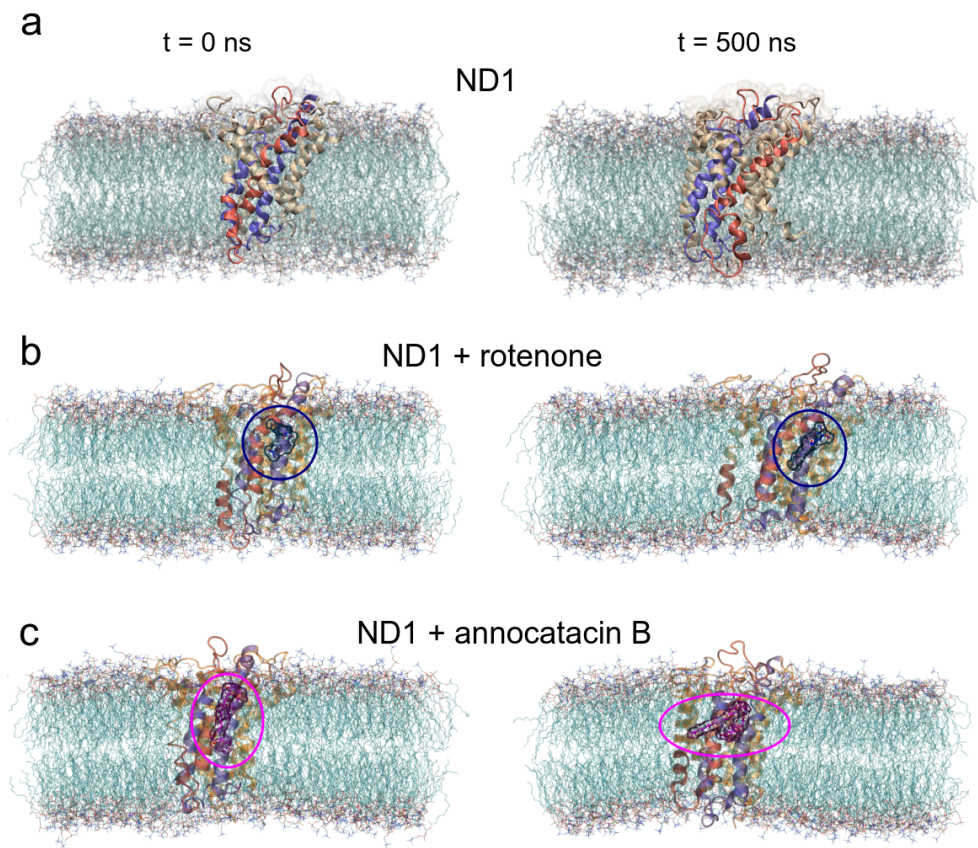258 annocatacin B complex (Table 3 and Figure 5a).

Figure 4. Overall structural organization of ND1 protein and its ligands in a membrane-embedded condition. The left panel shows the molecular complexes at initial conditions (0 *ns*). The right panel shows the complexes at 500 *ns*. (a) ND1 + DPPC membrane, (b) ND1 + DPCC + rotenone, and (c) ND1 + DPPC + annocatacin B.

Table 3: Stability Descriptors of the ND1 complexes.

System	Region	RMSD^a	RMSF^a	RG^a	H Bonds		
					Intra	Inter/Solv	Inter/Mem
	whole prot	0.40±0.02	0.19±0.09	2.12±0.01	209±9 (200)	338±15(336)	33±5(39)
ND1	Active site	0.30±0.05	0.13±0.04	1.91±0.01	89±6 (77)	166±10(165)	6±2(6)
	$y - axis$			1.74±0.03			
	whole prot	0.48±0.02	0.20±0.10	2.13±0.01	203±8(202)	356±13(356)	31±5(38)
ND1 + rotenone	Active site	0.41±0.11	0.14±0.07	1.90±0.02	84±6 (88)	176±10(174)	8±3(10)
	$y - axis$			1.70±0.04			
	whole prot	0.44±0.01	0.20±0.09	2.13±0.01	213±11 (207)	341±14(330)	26±5(23)
ND1 + annocatacin B	Active site	0.30±0.03	0.13±0.05	1.90±0.01	89±6 (81)	167±10(161)	5±3(2)
	$y - axis$			1.77±0.02			

^{a} In nanometers.

For H-bonds calculations, we considered determining those formed between ND1 subunit itself (intra); the ND1 subunit and solvent molecules (inter/solv); and the ND1 subunit and lipid bilayer membrane (inter/mem).
Values between parenthesis were calculated on global minimum energy structures obtained in the FEL analysis.
All values were obtained from the last 300 *ns* of the MD simulations.

259 In the case of the radii of gyration (RG), close values were obtained for the ND1-
260 ligand complexes (∼2.12 *nm*), due to the stability provided by the lipid membrane

261 (Table 3). Similarly, calculations performed in the active site showed few variations
262 among these zones in the three structures ($\sim$1.90 nm, Figure 5b). However, calculations
263 around the $y-axis$, showed that the most opened structure was the ND1 - annocatacin
264 B complex (1.77 $\pm$ 0.02 nm), being the ND1 - rotenone complex the most compacted
265 structure (1.70 $\pm$ 0.04 nm, Figure 5c).

266   Using both results, the active site RMSDs and $y-axis$ RG, we performed a free
267 energy landscape (FEL) analysis to obtain the minimal global energy conformations of
268 the ND1 complexes. The FEL maps showed the impact of ligands on the ND1 structure
269 stabilization. In Figure 5d, we can observe there is only a single conformation cluster
270 (dashed circles in the 2D maps), which indicates the great stability of the ND1 subunit in
271 the lipid membrane. In the case of the ligand complexes, there are four conformation
272 clusters that indicate the destabilization caused by the ligand molecules. However, the
273 location of these clusters was more close in the ND1 - annocatacin B complex (Figure
274 5e, Figure 5f). According to the results above, the 3D maps showed a large top area in
275 the ND1 - rotenone complex and a less top area in the annocatacin B complex, which
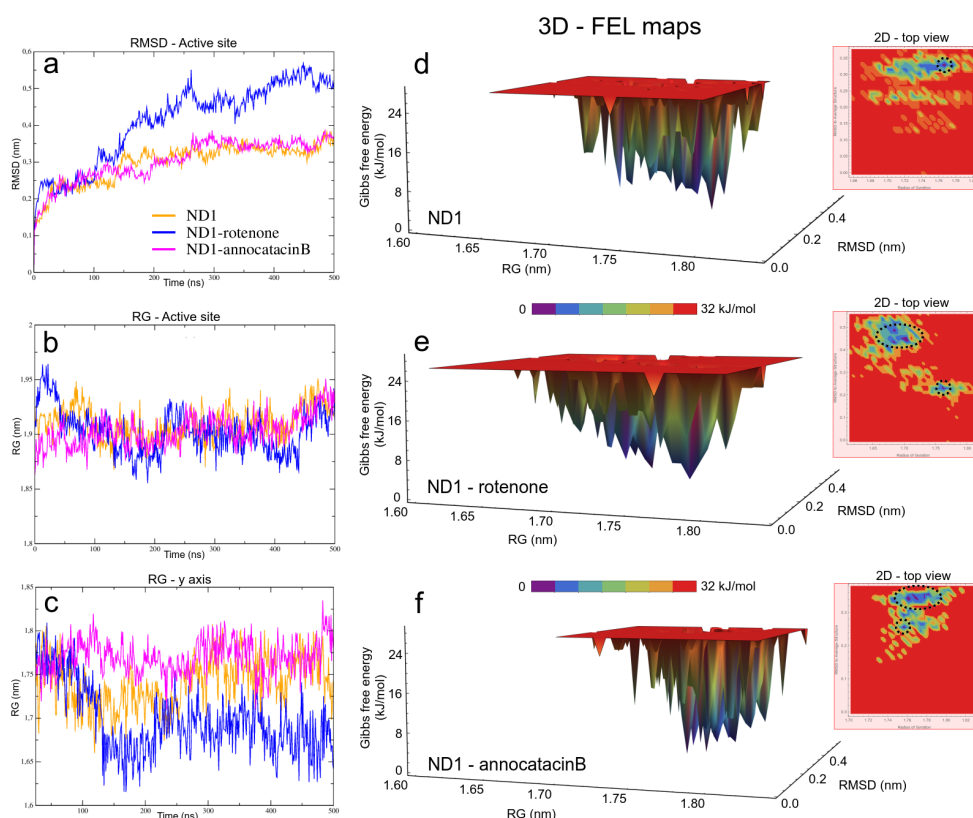276 suggests a more profound stabilization effect by annocatacin B on the ND1 subunit.

Figure 5. Structural analysis of the ND1 subunit active site. (a) RMSD; (b) RG; (c) RG on of $y-axis$ of the ND1 protein. The FEL maps (d, e, f) were built using structural coordinates from RMSD results and RG on the $y-axis$. The dash circles in the 2D plots indicate the global minimum energy structures showed in purple color in the 3D plots.

3.1.3. Hydrogen bond analysis

278   To elucidate this apparent contradiction between the results obtained from the
279 RMSD and RG analyses, we performed a hydrogen bonds (H-bond) analysis. Using the
280 *hbond* tool of Gromacs for the MD simulations, and the Hydrogen bonds plugin of VMD
281 for the global minimum energy structures, we obtained the H-bond interactions based on
282 a cutoff distance of 0.35 nm and a cutoff angle of 30°. Initially, we determined the H-bond
283 formation of the ND1 subunit, both, intra and intermolecular (Figure 6a, Table 3). The

284 results showed a greater intramolecular H-bonds formation in the ND1 - annocatacin B
285 complex (∼216) and its active site (∼89), but a decrease in the intermolecular interactions,
286 mainly with the lipid bilayer (∼26 and ∼5 for the active site). On the other hand, the
287 ND1-rotenone complex shows a maximum number of interactions with the solvent
288 molecules (∼356) and the most formation of H-bonds with the DPPC molecules (∼31
289 and 8 to active site). The same trend was presented in the case of the minimal energy
290 structures (parenthesis results). These results suggest that the annocatacin B increases
291 the intramolecular stability of the ND1 subunit contrary to the rotenone molecule, which
292 increases the intermolecular interactions mainly with the solvent molecules that are the
293 main cause of the protein instability.
294   To clarify these stability behaviors, we carried out H-bond calculations between
295 the ligand molecules and the system components. In Figure 6b, we can see the H-bond
296 formations of these ligands and all atoms in the molecular complexes. From a statistical
297 perspective at the last 200 *ns* of MD simulations, there are more H-bonds formations in
298 the annocatacin B complex (∼0.80) than the rotenone complex (∼0.42). Furthermore, the
299 analysis of the ND1 - ligand interactions (Figure 6c), showed almost exclusively ligand
300 interactions by annocatacin B on the ND1 subunit (∼0.15) versus rotenone interactions
301 (∼0.01). The results confirm that the annocatacin B stabilizes, in part, the ND1 structure
302 by polar interactions with its nearby residues. In order to identify the active site residues
303 involved in the stabilization interactions, we calculated the H-bond occupancies in the
304 MD simulations, and the Figure 6d shows the results obtained. In the case of the ND1
305 - rotenone complex, we can observe the greater occupancy value (9.95%) due to the
306 F223. However, only four residues were involved in the polar interactions (L222, F223,
307 A226, and T229). On the other hand, the ND1 - annocatacin B complex showed a major
308 number of polar interactions (14), being W185, F223, M233, and L237 residues that had
309 the highest number of occupancy values. Despite the hydrophobic character of the
310 ligand molecules, our H-bond analysis showed the importance of polar interactions in
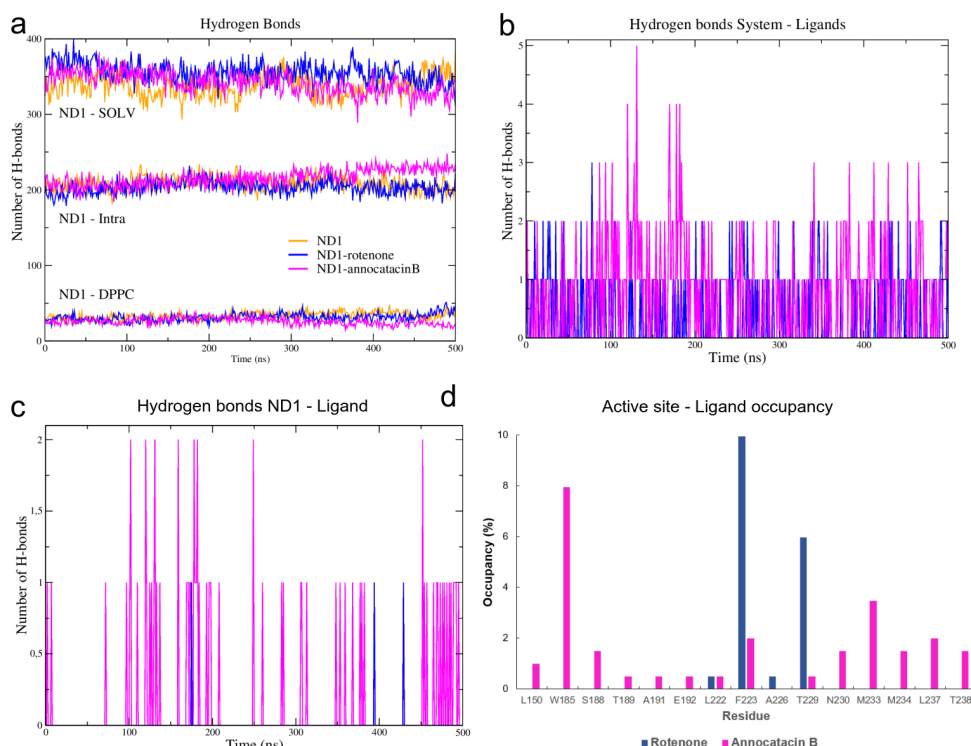311 the ND1 stabilization.

Figure 6. H-bond analysis of the ND1 complexes during 500 *ns* of the MD simulations.

3.1.4. RMSF and B-factor analysis

To evaluate local flexibilities of the ND1 subunit and describe the deviations of residues from the average position due to the ligand effects, we performed the root mean square fluctuation (RMSF) analysis. The main fluctuations of the ND1 protein were observed at the unembedded-loop regions, as expected (Table 3). Especially, high RMSF values were located between L33-G36 residues (ND1 - annocatacin B complex, $\sim$0.84 nm), and A249-S251 residues (ND1 - rotenone complex, $\sim$0.86 nm).

Despite the high stability of the active site, a fluctuations analysis was performed to understand the ligand effect in these region. For this purpose, in addition to RMSF calculations, we analyzed the B-factor, also called thermal factor or Debye-Walle factor [69] and we mapped the values on the active site surfaces.
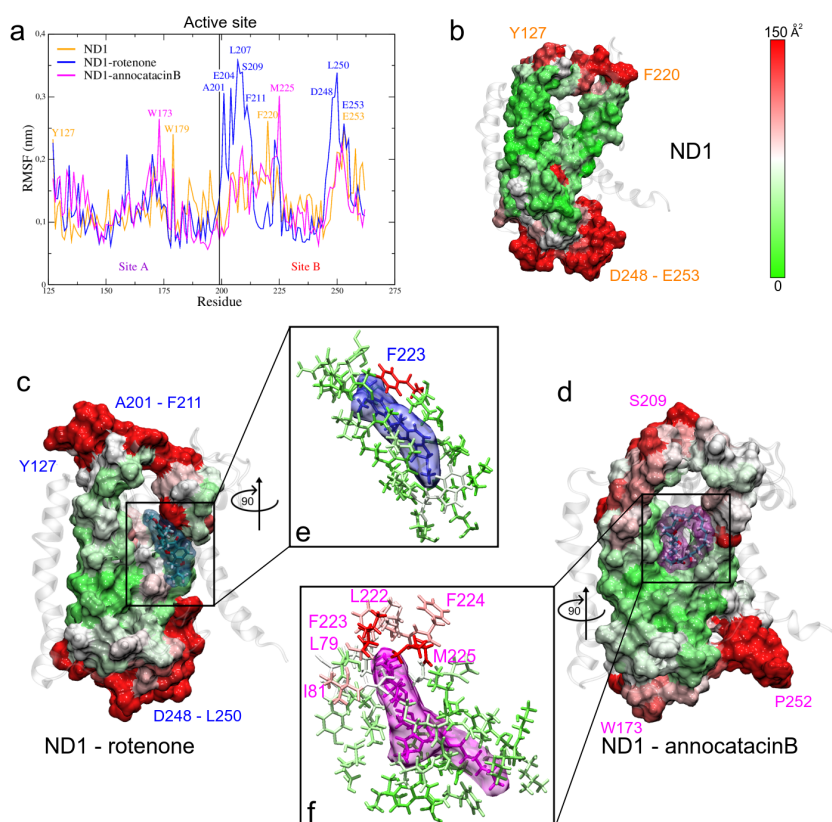

Figure 7. Fluctuation analysis of the ND1 residues. (a) RMSF plot of the active site residues obtained during the last 200 ns of the MD trajectories. (b, c, d) B-factor plotted on the molecular surface of the active site. The red color indicates high B factor values, whereas the green, low values. Ligands are shown in translucid surface, rotenone in blue color, and annocatacin B in magenta color. (e, f) Zoom of the ligand interactions.

The stable regions in the MD trajectories were used and the nearest neighbor residues B-factor values are shown in Table 4. The RMSF plot of the three systems shows that the ND1 - rotenone complex had the highest fluctuation (0.14 ± 0.06 nm), compared with the ND1 (0.13 ± 0.04 nm) and ND1 - annocatacin B (0.13 ± 0.05 nm) complexes (Figure 7a). In embedded active site regions, the ND1 subunit presents high stability, denoted by the green color of the B-factor surface (Figure 7b). However, this stability is altered by the presence of the ligand molecules making these regions more flexible. Figure 7c shows the rotenone effects on the neighbor residue fluctuations. The presence of white and red zones on the B-factor surface denotes a flexibility increase, especially, the F223 residue shows a high fluctuation value (144.4 Å). Figure 7d shows a zoom of rotenone and its influence zone on the ND1 protein, calculated at a minor distance of

0.5 *nm*. The interactions with 23 residues are observed in Table 4. On the other hand, the annocatacin B effects on the B-factor surface shows an increase in the number of residues with high fluctuation, being the L79 (179.7 Å) and M225 (231.7 Å) residues that had the highest fluctuation values (Figure 7e). Hence, the total number of residues interacting with the annocatacin B ligand were 37 (Figure 7f). The results suggest that the annocatacin B stabilizes the ND1 structure by size effect and by interaction with different domains out of the active site.

Finally, we included the SASA (Solvent Accessible Surface Area) value, that is an important descriptor of the ligand effects over the structure, in which ND1 - rotenone has a higher value (179.29 $\pm$ 1.47 nm^2) than ND1-annocatacin B (177.67 $\pm$ 1.53 nm^2) and ND1 without ligand (174.84 $\pm$ 1.37 nm^2).

Table 4: Contact analysis

System	Active Site				Other sites		
	Site A		**Site B**				
ND1 + rot + mem			L22(23) A226(14) N230(36) M233(20)	F223(144) T229(17) I232(10)	T73(21) A78(15) A82(18) W86(68) S115(23) S119(37)	A74(19) L79(45) L83(37) L89(30) I116(38)	L77(37) I81(20) L85(19) M91(23) W118(41)
ND1 + ann + mem	E143(39) W185(14) S188(13) A191(14)	L146(27) F186(41) T189(14) E192(15)	L222(94) F224(106) A226(70) T229(27) I231(37) M234(36)	F223(103) M225(232) E227(48) N230(25) M233(49) L237(50)	A78(102) A82(76) A112(40) S115(39) L266(28) F270(26)	L79(179) L85(43) V113(53) I116(70) T267(19) I273(49)	I81(101) S109(48) Y114(52) L117(74) L269(46)

Residues close to ligand at distance minor to 0.5 *nm* obtained at the last 200 *ns* of the MD trajectories.

In parenthesis, B-factor values.

3.1.5. MM electrostatic potential surfaces

As mentioned above, ND1 - ligand interactions mainly have a hydrophobic character and that is demonstrated by their drug-like properties. However, our results show an electrostatic contribution to structure stabilization. Thus, using the molecular mechanics APBS approximation [55], we calculated the ESP surfaces of ND1 subunit and their ligand complexes. For this purpose, we used the minimum energy structures and the Hirshfeld's atomic charges of the ligand molecules obtained in FEL analysis and QM calculations, respectively.

The electrostatic map of the ND1 structure shows a well-defined charged core surrounded by hydrophobic alpha-helices substructures. The core is formed mainly by the active site residues that confer a high negative charge to this region (T73-L117 and L266-I273, Figure 8a). We have observed that the binding domain comprises residues out of the active site and the electrostatic properties of these residues are affected by the ligand interactions. Figure 8b shows the drastic variations in the polar properties of the binding domain due to rotenone, increasing the positively charged regions. In addition, the binding domain seems to close, which would explain the more compactness observed in the radius of gyration analysis in this complex.
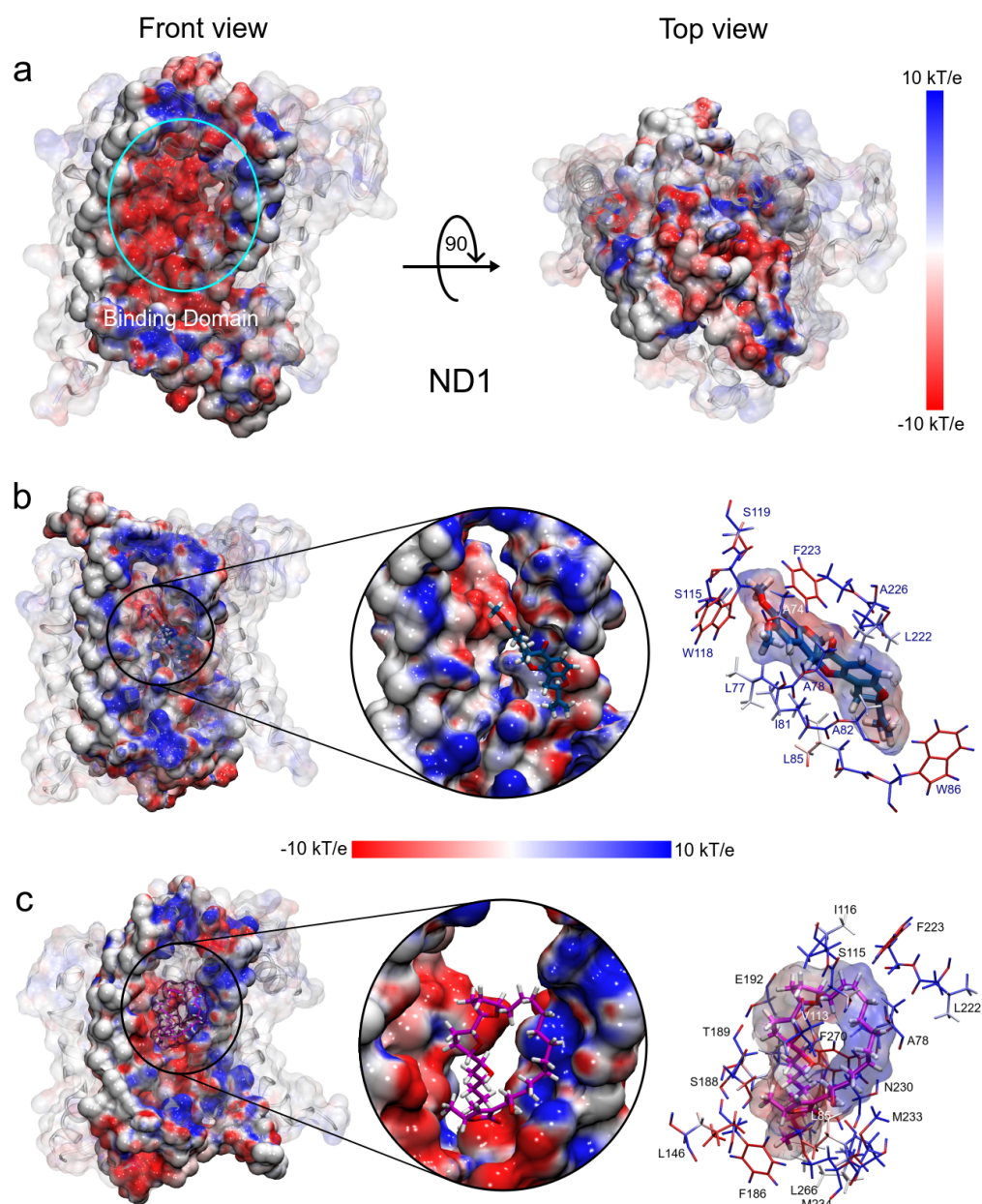
Figure 8. Electrostatic potential surfaces of molecular systems obtained with APBS. (a) ND1 protein structure. (b) ND1 - rotenone complex. (c) ND1 - annocatacin B complex. The red color indicates negatively charged regions and blue, positively charged. White color denotes hydrophobic regions.

On the other hand, the electrostatic changes observed by the annocatacin B presence in the binding domain were less dramatic, yet, conservating the negative polar character in most of its structure (Figure 8c). The main polar variations were located on the A78, S115, I116, L222, F223, N230, M233, and M234 residues, which increased their positive charge, doing this zone susceptible to nucleophilic attacks. These electrostatic variations suggest that the structural instability observed in the ND1 - rotenone complex can be due to structural changes in the active site.

3.2. Binding Free Energy

To analyze the energy properties of rotenone and annocatacin B when forming the ND1 - ligand complexes, we carried out MM/PBSA calculations based on the last 200

ns of the MD trajectories. In addition, an energy decomposition analysis per residue was performed to highlight the main residues that contribute to the stability of the complexes. As shown in Table 5, the binding free energy (BFE) of the two complexes was energetically favorable, however, the interaction energy of the ND1 - annocatacin B complex was more spontaneous (-333.18 $\pm$ 2.14 kJ/mol) than the rotenone complex (-218.15 $\pm$ 1.78 kJ/mol), which is according with that reported by Murai *et al.*, where they say that the inhibition potency of natural acetogenins is stronger than that of common synthetic inhibitors [22]. Due to the hydrophobic character of the ligand interactions, the main contributions to $\Delta G_{binding}$ energy were the van der Waals and nonpolar solvation terms. In both of them, the binding energy was more favorable to the annocatacin B interactions with the ND1 subunit ($\sim$39%). Furthermore, the electrostatic energy term confirms the polar contribution to the stability of the ND1 - ligand complexes as seen in the H-bond analysis, being higher in the annocatacin B complex. These results suggest that annocatacin B has a better stabilization effect on the whole ND1 structure.

Table 5: Average MM/PBSA free energies of ND1 complexes.

System	ΔE_{VW}^a	ΔE_{Elec}^b	ΔE_{PS}^c	ΔE_{SASA}^d	BFE^e
ND1-Annocatacin B	-358.76$\pm$1.26	-23.04$\pm$0.69	85.00$\pm$0.92	-36.38$\pm$0.10	-333.18$\pm$2.14
ND1-Rotenone	-219.81$\pm$0.89	-21.14$\pm$0.39	45.01$\pm$0.34	-22.21$\pm$0.06	-218.15$\pm$1.78

[a]Van der Waal energy.; [b]Electrostatic Energy,[c]Polar Solvation Energy; [d]SASA Energy; [e]Binding Free Energy
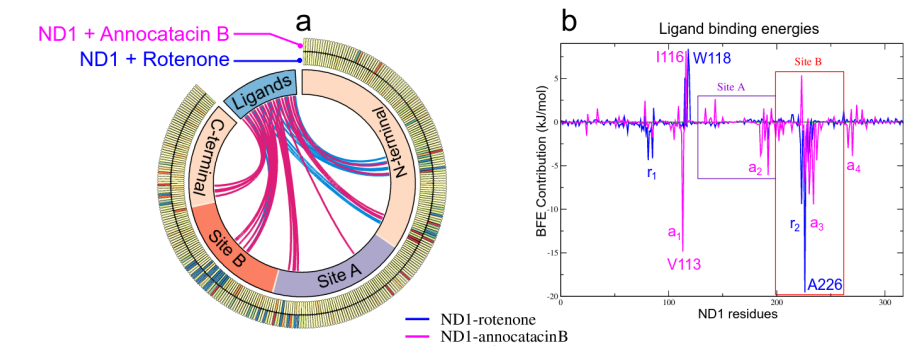All values are in $kJ.mol^{-1}$.

Figure 9. MM/PBSA analysis. (a) Circos plot representation of the ND1 - ligand structures,where the interactions of the ND1 subunit residues to the ligand molecules are shown as links inthe middle of the plot. The blue lines indicate interactions with rotenone and the magenta lines, with annocatacin B. The outer part of this plot shows the heat map of the BFE per residue, where blue color represents favorable BFE, red color unfavorable BFE, and yellow color indicates neutral energies. (b) Energy per-residue contributions plot.

As mentioned above, the ligand interactions involve, besides the active site, residues in other regions of the ND1 subunit allowing its structural stability. The large size of the annocatacin B molecule allows a greater number of energetically favorable contacts with these residues compared to those with which the rotenone molecule contacts (Figure 9a). The energy per-residue decomposition shows the different contributions to the binding strength in the ND1 - ligand complexes (Figure 9b). The highest binding free energy contribution was presented at active site B in the ND1 - rotenone complex with the A226 residue (-19.53 $\pm$ 0.24 kJ/mol). This complex showed two regions that favored the interactions with rotenone, namely r_1 (L79-L85) and r_2 (A221-M234), being r_2 a zone that involves H-bond interactions, what would explain its high contributions to the BFE. On the other hand, in the ND1 - annocatacin B complex, the greatest BFE contribution was with Val113 (-14.84 $\pm$ 0.54 kJ/mol), residue located outside the active

398 site and denoted as a_1. In addition, other three favorable regions were obtained in this
399 complex, namely a_2 (M184-T193), a_3 (A226-L237), and a_4 (L266-L271), which suggest
400 a better molecular coupling of annocatacin B into the ND1 protein. Table 6 shows the
401 residues that contributed the most to the BFE for both complexes.

Table 6: Top 10 residues that does contribute to the binding free energy

ND1- Rotetone	ΔE_{MM}	ΔE_{PS}	ΔE_{AS}	BFE
A226	-8.18±0.12	0.92±0.06	-12.27±0.19	-19.53±0.24
F223	-14.37±0.20	3.94±0.08	1.06±0.63	-9.41±0.60
I81	-9.21±0.11	0.66±0.02	4.19±0.14	-4.36±0.19
T229	-4.32±0.11	5.20±0.13	-5.06±0.32	-4.17±0.35
L85	-5.97±0.11	0.72±0.07	1.10±0.13	-4.15±0.16
N230	-1.35±0.06	0.72±0.06	-2.86±0.14	-3.49±0.16
L222	-9.03±0.10	2.46±0.07	3.79±0.18	-2.77±0.22
M225	-3.74±0.13	1.19±0.07	0.24±0.12	-2.31±0.13
M233	-2.77±0.07	2.23±0.07	-1.51±0.11	-2.05±0.13
E192	-1.61±0.08	-0.17±0.15	-0.22±0.01	-2.00±0.16
ND1- Annocatacin B				
V113	-12.39±0.22	2.74±0.12	-5.20±0.34	-14.84±0.54
M234	-10.30±0.16	3.67±0.08	-2.80±0.16	-9.43±0.24
N230	-10.59±0.19	6.10±0.13	-3.82±0.17	-8.30±0.25
A226	-4.94±0.22	0.60±0.08	-2.59±0.46	-6.92±0.61
E192	-8.48±0.20	1.29±0.35	1.11±0.22	-6.09±0.33
I231	-4.26±0.10	-0.19±0.02	-0.74±0.09	-5.19±0.13
E227	-0.98±0.26	-3.77±0.29	-0.35±0.10	-5.09±0.30
M233	9.20±0.16	4.13±0.08	0.61±0.09	-4.46±0.18
L237	-6.74±0.20	1.18±0.03	1.15±0.07	-4.40±0.19
F270	-7.34±0.16	1.39±0.06	2.06±0.10	-3.90±0.15

All values are in $kJ.mol^{-1}$

402   The positive energies in the BFE calculations are associated with unfavorable energy
403 interactions between the protein-ligand complexes, Table 7 shows the residues with the
404 highest positive values. In the rotenone complex, these residues were located previous
405 to the active site, namely S115, W118, and S119, being the W118 residue with the highest
406 energy value ($8.39 \pm 0.16\ kJ/mol$). On the other hand, in the annocatacin B complex,
407 we observed a greater amount of residues with positive values, being A116 (8.14 ± 0.15
408 kJ/mol), F223 ($5.35 \pm 0.19\ kJ/mol$), and E143 ($2.65 \pm 0.18\ kJ/mol$) the residues with
409 the most significant values. These results seem to indicate that size of annocatacin B
410 could also have a slight destabilizing effect on the ND1 structure, however, this effect is
411 counteracted by the favorable contributions that stabilize it.
412   Continuing with the BFE analysis, we used the minimum energy structures obtained
413 in the FEL analysis and the 2D ligand-protein interaction diagrams, in order to visualize
414 the moiety interactions of the ligand molecules. For this task, we plotted the BFE values
415 on the ND1 surfaces and analyzed the energy interactions on the ligand structures. In
416 the rotenone complex, we observed that the main residue interactions were located at the
417 dimethoxychromene moiety of rotenone. The greatest favorable interactions were A226
418 and F223 residues (dark blue color in Figure 10a), being this last one the residue that
419 more interactions showed with rotenone (up to 7 direct interactions with ND1 residues,
420 Figure 10b). Despite the numerous interactions (5), the energy of A82 residue was just
421 -1.04 $\pm$ 0.23 kJ/mol. Another important contributions to the BFE were I81, L85, T229,
422 and N230 residues that interacted with the pyranol and the dihydrofuran moieties of
423 the rotenone molecule, respectively. The rotenone's atom that involved the main energy

424 contributions was the oxygen of the hydroxyl group located at the pyranoloid ring.
425 Residues with the lowest contribution to the BFE were located on the methoxy groups,
426 being S115, W118, and S119 residues with high positive values. The non-polar solvation
427 contribution was the predominant energy term in these residues.

Table 7: Top 10 residues that does not contribute to the binding free energy

ND1- Rotetone	ΔE_{MM}	ΔE_{PS}	ΔE_{AS}	BFE
W118	-7.31±0.12	2.65±0.07	13.05±0.30	8.39±0.30
S119	-1.11±0.04	1.12±0.07	6.11±0.23	6.12±0.22
S115	-4.37±0.11	1.67±0.06	7.78±0.20	5.09±0.20
W86	-4.52±0.10	0.93±0.05	5.21±0.25	1.61±0.25
K262	1.14±0.01	-0.13±0.01	0.22±0.00	1.23±0.01
R195	1.61±0.03	-0.58±0.04	0.00±0.00	1.03±0.05
E214	1.53±0.03	-0.75±0.02	0.07±0.00	0.85±0.02
Y215	-0.47±0.02	0.41±0.03	0.91±0.12	0.84±0.13
A78	-9.30±0.11	2.64±0.06	7.37±0.23	0.71±0.29
E59	1.05±0.02	-0.30±0.01	-0.17±0.00	0.58±0.01
ND1- Annocatacin B				
I116	-3.78±0.09	0.51±0.03	11.40±0.24	8.14±0.23
F223	-4.83±0.13	2.67±0.15	7.50±0.25	5.35±0.30
E143	-7.08±0.23	8.98±0.56	0.70±0.10	2.65±0.52
A78	-3.20±0.08	2.23±0.09	3.42±0.15	2.44±0.16
R274	-1.97±0.13	4.04±0.10	-0.08±0.01	1.98±0.13
S109	-5.27±0.17	5.55±0.15	1.55±0.10	1.82±0.21
R134	1.12±0.02	0.65±0.03	-0.16±0.00	1.61±0.04
R195	0.83±0.04	0.74±0.03	0.01±0.00	1.59±0.04
R34	-0.24±0.06	1.88±0.06	-0.08±0.00	1.55±0.08
S188	-6.55±0.12	6.38±0.14	1.72±0.09	1.55±0.19

All values are in $kJ.mol^{-1}$.

428 In the case of the annocatacin B complex, the aliphatic chains of this ligand involve
429 the majority of the interactions with its amino acid environment. This includes the
430 interactions with V113 and I116, that were the main contribution and no-contribution
431 residues to the binding energy, respectively (Figure 10c, Figure 10d). The THF rings
432 only showed one interaction with S188 residue, being an unfavorable one to the total
433 BFE, nevertheless, the energy value was low ($1.55 \pm 0.54\ kJ/mol$). The γ-lactone ring
434 involved five interactions, three of them important contributors, namely N230 and M234
435 (-8.30 ± 0.25 and $-9.43 \pm 0.24\ kJ/mol$, respectively). The other two interactions with E143
436 and S188 residues represented unfavorable energies. Is interesting to note that although
437 the F223 residue showed high fluctuations in both molecular complexes, different energy
438 behavior was observed at the interactions with the ligand molecules. At the rotenone
439 complex, the interaction contributed favorably to the BFE with a significant value (-9.41
440 $\pm 0.60\ kJ/mol$), while at the annocatacin B complex, this contribution was unfavorable
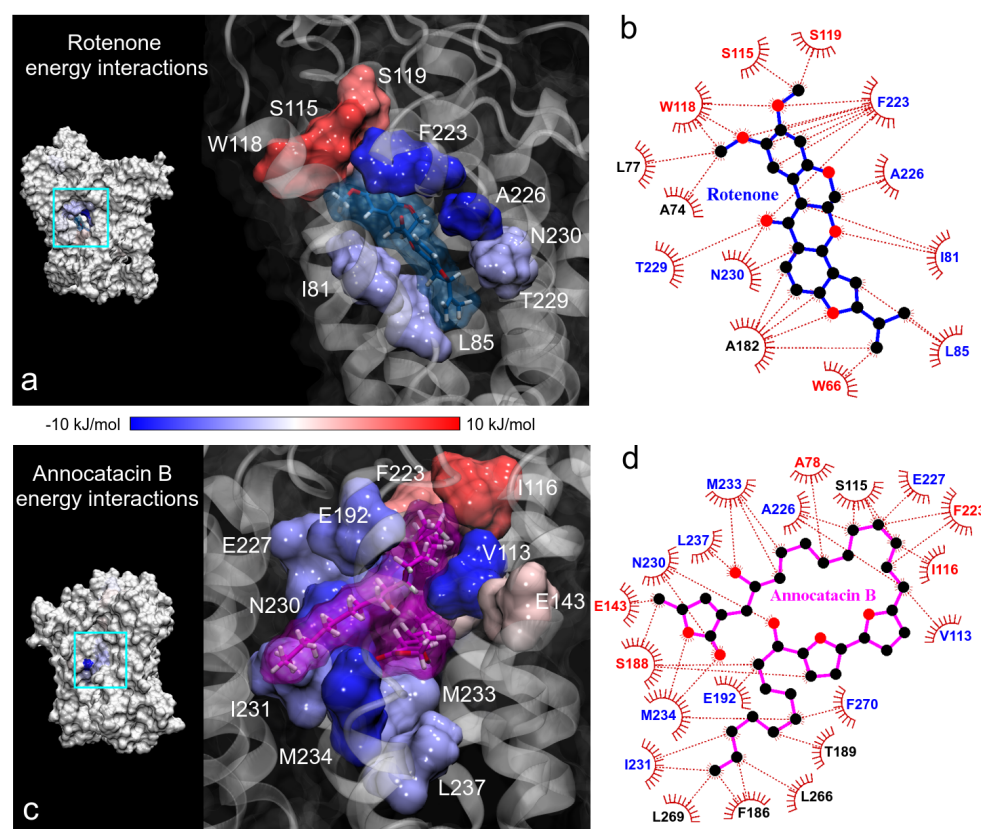441 ($5.35 \pm 0.30\ kJ/mol$).

Figure 10. Binding free energy (BFE) plotted on the ND1 surfaces. (a, c) 3D representation of the main residue contributions to BFE in the ND1 complexes. Blue color indicates favorable energies and red color unfavorable energies. (b,d) 2D representation of all interactions obtained in contact analysis in the minimum energy structures. The color of residue labels is the same as energy values.

4. Conclusions

QM optimizations, MD simulations, and MM/PBSA analyses were performed to evaluate the molecular and energetic complementarity of the annocatacin B molecule in the ND1 subunit of the human MRC-I. We compared this results with those obtained through the analysis of the ND1 - rotenone complex owing that the rotenone molecule is a powerful inhibitor of the activity of this MRC-I. Hirshfeld charges were used in the ligand molecules in order to not overestimate the electrostatic interactions within the molecular complexes. ND1 subunit is a transmembrane protein, thus we used a DPPC lipid bilayer as a membrane model for the entire simulations of the ND1 complexes in this work.

The overall analysis revealed a strong stabilizing effect of the annocatacin B molecule over the full ND1 protein structure. One of the essential reasons for this molecular stability could be the size and its capability of folding of annocatacin B, what ultimately allowed it to have more interactions with the ND1 nearby residues. Despite the hydrophobic nature of the ND1 - ligand interactions, we observed an increase in H-bonds formations in the ND1 - annocatacin B complex through the whole MD trajectory, this suggests a considerable electrostatic contribution to the stability of the complex. Another major consequence of these electrostatic effects was observed on the ESP surfaces at the active site; while annocatacin B retained the electrophilic pattern of the native active site of ND1, rotenone largely changed it to a nucleophilic one.

MM/PBSA analysis showed that the main energetic component of BFE was the hydrophobic interactions. Hence the important role of the aliphatic annocatacin B chains

in their affinity for the ND1 subunit. Several favorable interactions were observed
on these chains in the ND1 - annocatacin B complex, including residues outside the
active site (V113 and L266-L271), which allowed a better energetic coupling (35%) than
those observed in the ND1 - rotenone complex. A significant energy interaction was
observed with the F223 residue; in both ND1 - ligand complexes, this residue showed
high structural fluctuations. However, for the rotenone complex, the energy contribution
was favorable to the BFE (-9.41 $\pm$ 0.60 kJ/mol), whereas for the annocatacin B complex
the energy contribution of this residue was unfavorable (5.35 $\pm$ 0.30 kJ/mol). The reason
for this behavior could be that the residue F223 prefers electrostatic to hydrophobic
interactions.

Our results suggest that the natural annocatacin B molecule could display better
inhibitory capabilities than the rotenone molecule, an issue to be taken into account for
future research.

References

1. Warburg, O.H.; Dickens, F. _Metabolism of tumours_; Constable & Co. Ltd., 1930.
2. Ganapathy-Kanniappan, S.; Geschwind, J.F.H. Tumor glycolysis as a target for cancer therapy: progress and prospects. _Molecular cancer_ **2013**, _12_, 152.
3. Vander Heiden, M.G.; Cantley, L.C.; Thompson, C.B. Understanding the Warburg effect: the metabolic requirements of cell proliferation. _science_ **2009**, _324_, 1029–1033.
4. Wallace, D.C. Mitochondria and cancer. _Nature Reviews Cancer_ **2012**, _12_, 685.
5. Koppenol, W.H.; Bounds, P.L.; Dang, C.V. Otto Warburg's contributions to current concepts of cancer metabolism. _Nature Reviews Cancer_ **2011**, _11_, 325.
6. Smolková, K.; Plecitá-Hlavatá, L.; Bellance, N.; Benard, G.; Rossignol, R.; Ježek, P. Waves of gene regulation suppress and then restore oxidative phosphorylation in cancer cells. _The international journal of biochemistry & cell biology_ **2011**, _43_, 950–968.
7. Moreno-Sánchez, R.; Rodríguez-Enríquez, S.; Marín-Hernández, A.; Saavedra, E. Energy Substrate Modulates in tumor cells. _The FEBS journal_ **2007**, _274_, 1393–1418.
8. Jose, C.; Bellance, N.; Rossignol, R. Choosing between glycolysis and oxidative phosphorylation: a tumor's dilemma? _Biochimica et Biophysica Acta (BBA)-Bioenergetics_ **2011**, _1807_, 552–561.
9. Burlaka, A.; Ganusevich, I.; Vovk, A.; Burlaka, A.; Gafurov, M.; Lukin, S. Colorectal Cancer and Mitochondrial Dysfunctions of the Adjunct Adipose Tissues: A Case Study. _BioMed research international_ **2018**, _2018_.
10. Philley, J.V.; Kannan, A.; Qin, W.; Sauter, E.R.; Ikebe, M.; Hertweck, K.L.; Troyer, D.A.; Semmes, O.J.; Dasgupta, S. Complex-I alteration and enhanced mitochondrial fusion are associated with prostate cancer progression. _Journal of cellular physiology_ **2016**, _231_, 1364–1374.
11. Cormio, A.; Musicco, C.; Gasparre, G.; Cormio, G.; Pesce, V.; Sardanelli, A.M.; Gadaleta, M.N. Increase in proteins involved in mitochondrial fission, mitophagy, proteolysis and antioxidant response in type I endometrial cancer as an adaptive response to respiratory complex I deficiency. _Biochemical and biophysical research communications_ **2017**, _491_, 85–90.
12. Santidrian, A.F.; Matsuno-Yagi, A.; Ritland, M.; Seo, B.B.; LeBoeuf, S.E.; Gay, L.J.; Yagi, T.; Felding-Habermann, B. Mitochondrial complex I activity and NAD+/NADH balance regulate breast cancer progression. _The Journal of clinical investigation_ **2013**, _123_, 1068–1081.
13. Basit, F.; Van Oppen, L.M.; Schöckel, L.; Bossenbroek, H.M.; Van Emst-de Vries, S.E.; Hermeling, J.C.; Grefte, S.; Kopitz, C.; Heroult, M.; Willems, P.H. Mitochondrial complex I inhibition triggers a mitophagy-dependent ROS increase leading to necroptosis and ferroptosis in melanoma cells. _Cell death & disease_ **2017**, _8_, e2716.
14. Pamies, D.; Block, K.; Lau, P.; Gribaldo, L.; Pardo, C.A.; Barreras, P.; Smirnova, L.; Wiersma, D.; Zhao, L.; Harris, G. Rotenone exerts developmental neurotoxicity in a human brain spheroid model. _Toxicology and applied pharmacology_ **2018**, _354_, 101–114.

15. Chadderton, L.; Kelleher, S.; Brow, A.; Shaw, T.; Studholme, B.; Barrier, R. Testing the efficacy of rotenone as a piscicide for New Zealand pest fish species. Managing invasive freshwater fish in New Zealand. Proceedings of a workshop hosted by Department of Conservation, 2001, pp. 10–12.

16. Devi, P.; Shukla, V.; Meshram, Y. A review on the use of botanical pesticides in insect pest management. A review on the use of botanical pesticides in insect pest management, 2016.

17. Betarbet, R.; Sherer, T.B.; MacKenzie, G.; Garcia-Osuna, M.; Panov, A.V.; Greenamyre, J.T. Chronic systemic pesticide exposure reproduces features of Parkinson's disease. *Nature neuroscience* **2000**, *3*, 1301.

18. Li, N.; Ragheb, K.; Lawler, G.; Sturgis, J.; Rajwa, B.; Melendez, J.A.; Robinson, J.P. Mitochondrial complex I inhibitor rotenone induces apoptosis through enhancing mitochondrial reactive oxygen species production. *Journal of Biological Chemistry* **2003**, *278*, 8516–8525.

19. Cunningham, M.L.; Soliman, M.S.; Badr, M.Z.; Matthews, H. Rotenone, an anticarcinogen, inhibits cellular proliferation but not peroxisome proliferation in mouse liver. *Cancer letters* **1995**, *95*, 93–97.

20. Bhurtel, S.; Katila, N.; Srivastav, S.; Neupane, S.; Choi, D.Y. Mechanistic comparison between MPTP and rotenone neurotoxicity in mice. *Neurotoxicology* **2019**, *71*, 113–121.

21. Nopparat, C.; Porter, J.E.; Ebadi, M.; Govitrapong, P. 1-Methyl-4-phenylpyridinium-induced cell death via autophagy through a Bcl-2/Beclin 1 complex-dependent pathway. *Neurochemical research* **2014**, *39*, 225–232.

22. Murai, M.; Ishihara, A.; Nishioka, T.; Yagi, T.; Miyoshi, H. The ND1 subunit constructs the inhibitor binding domain in bovine heart mitochondrial complex I. *Biochemistry* **2007**, *46*, 6409–6416.

23. Chen, Y.; Chen, J.w.; Zhai, J.h.; Wang, Y.; Wang, S.l.; Li, X. Antitumor activity and toxicity relationship of annonaceous acetogenins. *Food and chemical toxicology* **2013**, *58*, 394–400.

24. Patel, M.S.; Patel, J.K. A review on a miracle fruits of Annona muricata. *Journal of Pharmacognosy and Phytochemistry* **2016**, *5*, 137.

25. Moghadamtousi, S.; Fadaeinasab, M.; Nikzad, S.; Mohan, G.; Ali, H.; Kadir, H. Annona muricata (Annonaceae): a review of its traditional uses, isolated acetogenins and biological activities. *International journal of molecular sciences* **2015**, *16*, 15625–15658.

26. Prasad, S.K.; Varsha, V.; Devananda, D. Anti-cancer properties of Annona muricata (L.): A Review. *Medicinal Plants-International Journal of Phytomedicines and Related Industries* **2019**, *11*, 123–134.

27. Gavamukulya, Y.; Wamunyokoli, F.; El-Shemy, H.A. Annona muricata: Is the natural therapy to most disease conditions including cancer growing in our backyard? A systematic review of its research history and future prospects. *Asian Pacific journal of tropical medicine* **2017**, *10*, 835–848.

28. Zafra-Polo, M.C.; González, M.C.; Estornell, E.; Sahpaz, S.; Cortes, D. Acetogenins from Annonaceae, inhibitors of mitochondrial complex I. *phytochemistry* **1996**, *42*, 253–271.

29. Mangal, M.; Imran Khan, M.; Mohan Agarwal, S. Acetogenins as potential anticancer agents. *Anti-Cancer Agents in Medicinal Chemistry (Formerly Current Medicinal Chemistry-Anti-Cancer Agents)* **2016**, *16*, 138–159.

30. Chang, F.R.; Liaw, C.C.; Lin, C.Y.; Chou, C.J.; Chiu, H.F.; Wu, Y.C. New adjacent bis-tetrahydrofuran annonaceous acetogenins from Annona muricata. *Planta medica* **2003**, *69*, 241–246.

31. Dennington, R.; Keith, T.A.; Millam, J.M. GaussView 6.0. 16. *Semichem Inc.: Shawnee Mission, KS, USA* **2016**.

32. Frisch, M.J.; Trucks, G.W.; Schlegel, H.B.; Scuseria, G.E.; Robb, M.A.; Cheeseman, J.R.; Scalmani, G.; Barone, V.; Petersson, G.A.; Nakatsuji, H.; Li, X.; Caricato, M.; Marenich, A.V.; Bloino, J.; Janesko, B.G.; Gomperts, R.; Mennucci, B.; Hratchian, H.P.; Ortiz, J.V.; Izmaylov, A.F.; Sonnenberg, J.L.; Williams-Young, D.; Ding, F.; Lipparini, F.; Egidi, F.; Goings, J.; Peng, B.; Petrone, A.; Henderson, T.; Ranasinghe, D.; Zakrzewski, V.G.; Gao, J.; Rega, N.; Zheng, G.; Liang, W.; Hada, M.; Ehara, M.; Toyota, K.; Fukuda, R.; Hasegawa, J.; Ishida, M.; Nakajima, T.; Honda, Y.; Kitao, O.; Nakai, H.; Vreven, T.; Throssell, K.; Montgomery, Jr., J.A.; Peralta, J.E.; Ogliaro, F.; Bearpark, M.J.; Heyd, J.J.; Brothers, E.N.; Kudin, K.N.; Staroverov, V.N.; Keith, T.A.; Kobayashi, R.; Normand, J.; Raghavachari, K.; Rendell, A.P.; Burant, J.C.; Iyengar, S.S.; Tomasi, J.; Cossi, M.; Millam, J.M.; Klene, M.; Adamo, C.; Cammi, R.; Ochterski, J.W.; Martin, R.L.; Morokuma, K.; Farkas, O.; Foresman, J.B.; Fox, D.J. Gaussian~16 Revision C.01, 2016. Gaussian Inc. Wallingford CT.

33. Yanai, T.; Tew, D.P.; Handy, N.C. A new hybrid exchange-correlation functional using the Coulomb-attenuating method (CAM-B3LYP). *Chemical Physics Letters* **2004**, *393*, 51–57. doi:10.1016/j.cplett.2004.06.011.

34. Schäfer, A.; Huber, C.; Ahlrichs, R. Fully optimized contracted Gaussian basis sets of triple zeta valence quality for atoms Li to Kr. *The Journal of Chemical Physics* **1994**, *100*, 5829–5835. doi:10.1063/1.467146.

35. Hirshfeld, F.L. Bonded-atom fragments for describing molecular charge densities. *Theoretica chimica acta* **1977**, *44*, 129–138.

36. Ritchie, J.P. Electron density distribution analysis for nitromethane, nitromethide, and nitramide. *Journal of the American Chemical Society* **1985**, *107*, 1829–1837.

37. Ritchie, J.P.; Bachrach, S.M. Some methods and applications of electron density distribution analysis. *Journal of Computational Chemistry* **1987**, *8*, 499–509.

38. Mikhailovich, K.P. ERG Research Group. http://erg.biophys.msu.ru/tpp/, 2008. Accessed 28-04-2021.

39. Jorgensen, W.L.; Maxwell, D.S.; Tirado-Rives, J. Development and testing of the OPLS all-atom force field on conformational energetics and properties of organic liquids. *Journal of the American Chemical Society* **1996**, *118*, 11225–11236.

40. Kaminski, G.A.; Friesner, R.A.; Tirado-Rives, J.; Jorgensen, W.L. Evaluation and reparametrization of the OPLS-AA force field for proteins via comparison with accurate quantum chemical calculations on peptides. *The Journal of Physical Chemistry B* **2001**, *105*, 6474–6487.

41. Kandt, C.; Ash, W.L.; Tieleman, D.P. Setting up and running molecular dynamics simulations of membrane proteins. *Methods* **2007**, *41*, 475–488.

42. Guo, R.; Zong, S.; Wu, M.; Gu, J.; Yang, M. Architecture of human mitochondrial respiratory megacomplex I2III2IV2. *Cell* **2017**, *170*, 1247–1257.

43. Pettersen, E.F.; Goddard, T.D.; Huang, C.C.; Couch, G.S.; Greenblatt, D.M.; Meng, E.C.; Ferrin, T.E. UCSF Chimera—a visualization system for exploratory research and analysis. *Journal of computational chemistry* **2004**, *25*, 1605–1612.

44. Van Der Spoel, D.; Lindahl, E.; Hess, B.; Groenhof, G.; Mark, A.E.; Berendsen, H.J. GROMACS: fast, flexible, and free. *Journal of computational chemistry* **2005**, *26*, 1701–1718.

45. Tieleman, D.; Van der Spoel, D.; Berendsen, H. Molecular dynamics simulations of dodecylphosphocholine micelles at three different aggregate sizes: micellar structure and chain relaxation. *The Journal of Physical Chemistry B* **2000**, *104*, 6380–6388.

46. Duhovny, D.; Nussinov, R.; Wolfson, H.J. Efficient unbound docking of rigid molecules. International workshop on algorithms in bioinformatics. Springer, 2002, pp. 185–200.

47. Schneidman-Duhovny, D.; Inbar, Y.; Nussinov, R.; Wolfson, H.J. PatchDock and SymmDock: servers for rigid and symmetric docking. *Nucleic acids research* **2005**, *33*, W363–W367.

48. Homeyer, N.; Gohlke, H. Free energy calculations by the molecular mechanics Poisson- Boltzmann surface area method. *Molecular informatics* **2012**, *31*, 114–122.

49. Kumari, R.; Kumar, R.; Consortium, O.S.D.D.; Lynn, A. g_mmpbsa A GROMACS tool for high-throughput MM-PBSA calculations. *Journal of chemical information and modeling* **2014**, *54*, 1951–1962.

50. Brown, S.P.; Muchmore, S.W. Large-scale application of high-throughput molecular mechanics with Poisson- Boltzmann surface area for routine physics-based scoring of protein- ligand complexes. *Journal of medicinal chemistry* **2009**, *52*, 3159–3165.

51. Rastelli, G.; Rio, A.D.; Degliesposti, G.; Sgobba, M. Fast and accurate predictions of binding free energies using MM-PBSA and MM-GBSA. *Journal of computational chemistry* **2010**, *31*, 797–810.

52. Humphrey, W.; Dalke, A.; Schulten, K. VMD: visual molecular dynamics. *Journal of molecular graphics* **1996**, *14*, 33–38.

53. Turner, P.; Grace, X. *Version 5.1. 19. Center for Coastal and Land-margin Research*; Oregon Graduate Institute of Science and Technology Beaverton, OR, 2005.

54. Wallace, A.C.; Laskowski, R.A.; Thornton, J.M. LIGPLOT: a program to generate schematic diagrams of protein-ligand interactions. *Protein engineering, design and selection* **1995**, *8*, 127–134.

55. Baker, N.A.; Sept, D.; Joseph, S.; Holst, M.J.; McCammon, J.A. Electrostatics of nanosystems: application to microtubules and the ribosome. *Proceedings of the National Academy of Sciences* **2001**, *98*, 10037–10041.

56. Dolinsky, T.J.; Nielsen, J.E.; McCammon, J.A.; Baker, N.A. PDB2PQR: an automated pipeline for the setup of Poisson–Boltzmann electrostatics calculations. *Nucleic acids research* **2004**, *32*, W665–W667.

57. Kakutani, N.; Murai, M.; Sakiyama, N.; Miyoshi, H. Exploring the Binding Site of Δlac-Acetogenin in Bovine Heart Mitochondrial NADH- Ubiquinone Oxidoreductase. *Biochemistry* **2010**, *49*, 4794–4803.

58. Inc., W.R. Mathematica, Version 12.1. Champaign, IL, 2020.

59. Lobo-Jarne, T.; Ugalde, C. Respiratory chain supercomplexes: Structures, function and biogenesis. Seminars in cell & developmental biology. Elsevier, 2018, Vol. 76, pp. 179–190.

60. Fedor, J.G.; Hirst, J. Mitochondrial supercomplexes do not enhance catalysis by quinone channeling. *Cell metabolism* **2018**, *28*, 525–531.

61. Fiedorczuk, K.; Letts, J.A.; Degliesposti, G.; Kaszuba, K.; Skehel, M.; Sazanov, L.A. Atomic structure of the entire mammalian mitochondrial complex I. *Nature* **2016**, *538*, 406.

62. Nakanishi, S.; Abe, M.; Yamamoto, S.; Murai, M.; Miyoshi, H. Bis-THF motif of acetogenin binds to the third matrix-side loop of ND1 subunit in mitochondrial NADH-ubiquinone oxidoreductase. *Biochimica et Biophysica Acta (BBA)-Bioenergetics* **2011**, *1807*, 1170–1176.

63. Pérez de la Luz, A.; Aguilar-Pineda, J.A.; Méndez-Bermúdez, J.G.; Alejandre, J. Force field parametrization from the Hirshfeld molecular electronic density. *Journal of chemical theory and computation* **2018**, *14*, 5949–5958.

64. Riquelme, M.; Lara, A.; Mobley, D.L.; Verstraelen, T.; Matamala, A.R.; Vohringer-Martinez, E. Hydration free energies in the FreeSolv database calculated with polarized iterative Hirshfeld charges. *Journal of chemical information and modeling* **2018**, *58*, 1779–1797.

65. Ishizuka, R.; Matubayasi, N. Effective charges of ionic liquid determined self-consistently through combination of molecular dynamics simulation and density-functional theory. *Journal of computational chemistry* **2017**, *38*, 2559–2569.

66. Gastegger, M.; Marquetand, P. Molecular dynamics with neural network potentials. In *Machine Learning Meets Quantum Physics*; Springer, 2020; pp. 233–252.

67. Llanos, A.G.; Vöhringer-Martinez, E. pKa Calculations of Asp26 in Thioredoxin with Alchemical Free Energy Simulations and Hirshfeld-I Atomic Charges, 2018.

68. Pires, D.E.; Blundell, T.L.; Ascher, D.B. pkCSM: predicting small-molecule pharmacokinetic and toxicity properties using graph-based signatures. *Journal of medicinal chemistry* **2015**, *58*, 4066–4072.

69. Pang, Y.P. Use of multiple picosecond high-mass molecular dynamics simulations to predict crystallographic B-factors of folded globular proteins. *Heliyon* **2016**, *2*, e00161.